Available online at www.sciencedirect.com
ScienceDirect
International Journal of Heat and Fluid Flow 28 (2007) 407–417
International Journal of HEAT AND FLUID FLOW
www.elsevier.com/locate/ijhff

The evaporation of a saturated porous layer inside an inclined airflow channel

Yin Chou, Ruey-Jen Yang *

Department of Engineering Science, National Cheng Kung University, 1 University Road, Tainan 70101, Taiwan

Received 24 November 2005; received in revised form 3 March 2006; accepted 21 April 2006
Available online 24 July 2006

Abstract

This study investigates the enhancement in the heat and mass transfer of liquid film evaporation obtained by introducing a liquid-saturated porous layer within an inclined flow channel. The liquid and air streams are modeled as two coupled laminar boundary layers incorporating non-Darcian models of the inertia and boundary effects and the numerical solution is obtained by means of a fully implicit finite difference method. The effects of the porosity (ε), porous layer thickness (δ), inclined angle (φ), ambient relative humidity (ϕ) and Lewis number (Le) on the average heat and mass transfer performance are thoroughly examined. It is found that the porous layer enhances the heat and mass transfer performance. Specifically, the numerical results indicate that the average Nusselt number (Nu) and the Sherwood number (Sh) both increase with increasing φ, with decreasing ε and δ .The increase in ϕ results in the decreasing in Nu and increasing in Sh. Additionally, the influence of the porosity (ε) on the heat and mass transfer performance becomes more significant as the thickness of the inclined angle (φ) decreases.

Keywords: Liquid film evaporation; Porous medium; Heat and mass transfer

1. Introduction

Liquid film evaporation is an effective latent heat transfer mechanism widely utilized in the field of energy for many different applications, including chemical distillation, air conditioning, cooling towers, drying, desalination, and so forth. The physical scheme for liquid film evaporation consists of a thin liquid film flowing down a heated plate, with the liquid film exposed to a forced air stream. Since part of the liquid evaporates into the air stream, liquid film evaporation has a high heat transfer coefficient, low feed rates and another specific advantage of liquid film evaporation. However, conducting a theoretical analysis of the liquid film evaporation problem is complicated because the transport phenomena involve coupled heat and mass transfer at the liquid film-air interface.

Previous studies generally examined the liquid film evaporation problem using simplified 1-D or 2-D mathematical models. For example, a 1-D model was used to develop the governing equations for mass, mass species, momentum and energy conservation by applying the conservation laws to control volumes of the liquid film and the moist air (Maclaine-Cross and Banks, 1972, 1981; Wassel and Mills, 1987; Peres-Blanco and Bird, 1984). Maclaine-Cross and Banks (1972, 1981) analyzed the heat and mass transfer characteristics in a wet surface heat exchanger. Their theoretical results were found to be 20% higher than the corresponding experimental data. Wassel and Mills (1987) presented a 1-D design methodology for a counter-current falling film evaporative cooler. Their results indicated that narrow flow passages were more effective than conventional designs in improving the thermal performance of the evaporative condenser. A 1-D model of heat and mass transfer in a vertical single-tube exchanger was formulated by Peres-Blanco and Bird (1984). Early studies using 2-D models to investigate heat and mass transfer in an air

* Corresponding author. Tel.: +886 6 200 2724.
E-mail address: rjyang@mail.ncku.edu.tw (R.-J. Yang).

0142-727X/$ - see front matter © 2006 Elsevier Inc. All rights reserved.
doi:10.1016/j.ijheatfluidflow.2006.04.007

Nomenclature

C	inertia coefficient
d	thickness of porous layer (m)
d_p	particle diameter (m)
D	mass diffusivity ($m^2\ s^{-1}$)
Da	Darcy number $Da = K/d^2$
Fr	Froude number $Fr = U_{g,ave}/(gH\cos\varphi)^{1/2}$
g	gravitational acceleration ($m\ s^{-2}$)
H	channel width (m)
$h_{t,x}$	local heat transfer coefficient ($W\ m^{-2}\ °C^{-1}$)
$h_{m,x}$	local mass transfer coefficient ($m\ s^{-1}$)
h_{fg}	latent heat of vaporization ($J\ kg^{-1}$)
K	permeability of the porous layer (m^2)
k	thermal conductivity ($W\ m^{-1}\ °C^{-1}$)
L	plate length (m)
Le	Lewis number, $Le = \alpha/D$
M	molar mass ($kg\ mol^{-1}$)
m''_v	vapor mass flux ($kg\ m^{-2}\ s^{-1}$)
Nu	average Nusselt number
Nu_x	local Nusselt number
P	pressure (Pa)
Pr	Prandtl number
q''_l	latent heat flux ($W\ m^{-2}$)
q''_s	sensible heat flux ($W\ m^{-2}$)
Re_g	air Reynolds number, $Re_g = u_{g,ave}H/\nu_g$
Sh	average Sherwood number
Sh_x	local Sherwood number
T	temperature (°C)
U, V	dimensionless velocity
u, v	velocity along x, y coordinates ($m\ s^{-1}$)
X, Y	dimensionless coordinates
x, y	coordinate (m)

Greek symbols

α	effective thermal diffusivity ($m^2\ s^{-1}$)
δ	dimensionless thickness of porous layer
ε	porosity
θ	dimensionless temperature, $\theta = (T - T_w)/(T_{in} - T_w)$
Γ	dimensionless inertia coefficient of porous medium, $\Gamma = Cu_{g,ave}\sqrt{K}/\nu_l$
λ	dimensionless concentration, $\lambda = (\omega - \omega_\infty)/(\omega_w - \omega_\infty)$
τ	shear stress (Pa)
μ	dynamic viscosity ($kg\ s^{-1}\ m^{-1}$)
ν^*	kinematic viscosity ratio of liquid to air
ρ	mass density ($kg\ m^{-3}$)
φ	inclined angle
ϕ	relative humidity at inlet
ω	relative humidity

Subscripts

ave	average velocity of air stream at inlet
e	effective parameter of porosity
g	air stream
i	liquid–air interface
l	liquid film
w	wall
∞	inlet or free stream condition

stream assumed the liquid film to be at rest and to have a very thin constant thickness. In these studies, the vaporizing liquid film was treated as the boundary condition for the air stream (e.g. Gebhart and Pera, 1971 and Chen and Yuh, 1979) and the temperature distribution across the film was assumed to be linear (e.g. Shembharkar and Pai, 1986; Baumann and Thiele, 1990).

Recently, researchers have proposed more rigorous treatments of the equations governing the liquid film and the liquid–air interface. Yan and Lin (1991) studied the evaporative cooling of liquid films through interfacial heat and mass transfer mechanisms in a vertical channel. Yan and Soong (1995) presented a numerical solution for convective heat and mass transfer along an inclined heated plate with film evaporation. Tsay (1995) numerically analyzed the cooling characteristics of a wet surface heat exchanger with a liquid film evaporating into a countercurrent moist air steam. However, these studies neglected inertia effects in the momentum equation and the transverse convection term in the heat equation, and therefore the liquid film flow simplified to a 1-D momentum equation and a 1-D (or 2-D) heat equation. Mezaache and Daguenet (2005) developed a comprehensive two-dimensional boundary layer model for the evaporating liquid and air steam along an inclined plate. Their parametric study focused on the individual and combined effects of the air velocity, the liquid mass flow rate and the inclined angle on the heat and mass transfer performance in airflow channels with isothermal and heated walls, respectively. Their results indicated that a higher liquid mass flow rate and a lower air velocity increased the effect of the inclined angle on the heat and mass transfer rate.

From the discussions above, it is clear that previous theoretical research in evaporating liquid film flow has focused primarily on the effects of the inlet and geometrical conditions on the coupled heat and mass transfer characteristics. Moreover, these analyses all considered the flow of a liquid film over a flat solid surface. However, more recent studies have explored various techniques for enhancing the heat and mass transfer performance of liquid film evaporation. For example, various researchers have roughened the surface either randomly with sand grains or by adding regular geometric roughness elements such as ribs or rods etc. onto the surface (Han et al., 1978; Dowson and Trass, 1972; Kozlu et al., 1992; Zheng and Worek, 1996). These studies focused on developing accurate predictions of the flow

behavior for a given roughness geometry and establishing the optimum geometry for a given flow friction. In an alternative approach, some researchers utilized a porous structure composite for the plate in the flow channel to provide a large contact area, thereby increasing the heat and mass transfer (Zhao, 1999; Diky et al., 1996). Zhao (1999) studied coupled heat and mass transfer in a stagnation point flow of air through a heated porous bed with liquid film evaporation. In establishing the analytical solution, it was assumed that the liquid layer was very thin and stationary, and the air stream was idealized as having a stagnation point flow pattern. Diky et al., 1996 carried out an experimental investigation into liquid film evaporation in a heated air steam in a contact apparatus with a porous packing.

From the discussions above, it appears that the literature lacks theoretical investigations into the feasibility of utilizing porous materials to enhance the heat and mass transfer performance in falling liquid evaporation. Part of the reason for this is that the coupled heat and mass transfer process becomes more complicated in the presence of a porous medium. Accordingly, the present study analyzes liquid film evaporation flow along an inclined channel covered with a thin liquid-saturated porous layer. A two-dimensional steady laminar boundary layer model is adopted for the air and liquid streams. In developing the model, non-Darcian inertia and boundary effects are incorporated into the governing equations of the liquid-saturated porous medium. The governing equations are discretized to a fully implicit difference representation and solved using the tridiagonal matrix method. The principal objective of this study is to evaluate the effect of a liquid-saturated porous layer on the heat and mass transfer characteristics of liquid film evaporation flow. Specifically, this study investigates the influence of parameters such as the air inlet conditions (e.g. the Reynolds number and the ambient relative humidity) and the structural properties of the porous material (e.g. the porosity and thickness of the porous layer) on the performance of the liquid film evaporation.

2. Mathematical formulation

As shown schematically in Fig. 1, the current problem considers an inclined 2-D channel between two parallel plates. The lower plate is covered by a porous layer and which is wetted by a falling liquid film with an inlet temperature $T_{l,in}$ and an inlet flow rate $m_{l,in}$. The liquid film is exposed to a co-current forced air steam with a free stream velocity $u_{g,\infty}$, an ambient temperature $T_{g,\infty}$, and a relative humidity ω_∞. The plate is coated with a thin porous layer of thickness d. Heat is transferred from the plate to the liquid film and subsequently to the air stream, which is assumed to have a laminar and steady flow. The continuity of the shear stress boundary condition is assumed at the interface of the air and liquid films. The mass and heat flux produced by both temperature and concentration gradients

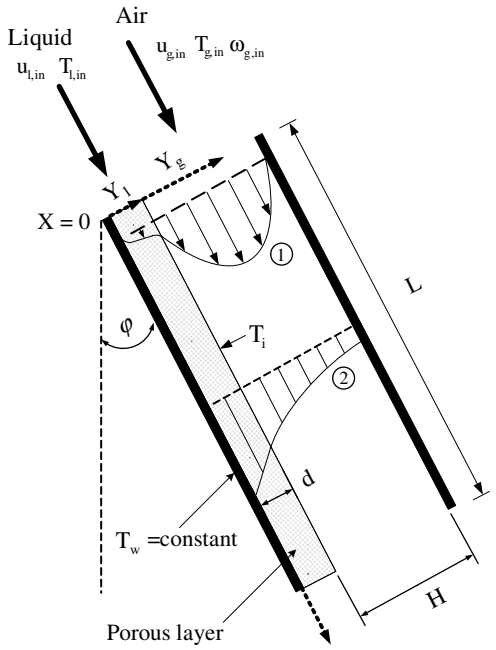

Fig. 1. Schematic diagram of physical system: ① Velocity profile; ② Temperature profile.

in the flow field are assumed to be small so that the Soret and Dufour effects are neglected in the present analyses. Finally, it is assumed that the liquid-saturated porous medium is isotropic and homogeneous and that the liquid is in local thermal equilibrium with the porous medium. Based on the above assumptions, we make use of two coordinate systems (x, y_l) and (x, y_g) referring to liquid side and air side respectively. Note that at $y_l = d$ is corresponding to $y_g = 0$. The governing equations for the liquid-film and air stream regions, and the corresponding boundary conditions, are developed as follows:

(a) *Liquid film region*

Under the assumptions of constant physical properties, no viscous dissipation, no internal heat generation, the laminar and steady 2-D boundary layer equations for liquid film flow in porous medium have been derived by Alazmi and Vafai (2000). Adopting non-Darcian models and neglecting transverse velocity component v_l due to fully-developed, the laminar axial momentum and energy boundary layer equations can be further simplified as

$$0 = \rho_l g \cos\varphi + \frac{\mu_l}{\varepsilon}\frac{\partial^2 u_l}{\partial y_l^2} - \frac{\mu_l}{K}u_l - \frac{\rho_l C}{\sqrt{K}}u_l^2 \tag{1}$$

$$u_l \frac{\partial T_l}{\partial x} = \alpha_e \frac{\partial^2 T_l}{\partial y_l^2} \tag{2}$$

where the subscript "l" denotes liquid stream variables, φ is the inclined angle, K is the permeability of the porous medium, C is the flow inertia parameter (Alazmi and Vafai (2000)), ε is the porosity and α_e is the effective thermal diffusivity ($\alpha_e = k_e/\rho_l C_{p,l}$). The effective thermal conductivity k_e is defined as $k_e = \varepsilon\, k_l + (1-\varepsilon)k_{solid}$.

(b) *Air stream region*

The two-dimensional laminar continuity, momentum, energy and concentration equations can be written as

$$\frac{\partial u_g}{\partial x}+\frac{\partial v_g}{\partial y_g}=0 \tag{3}$$

$$u_g\frac{\partial u_g}{\partial x}+v_g\frac{\partial u_g}{\partial y_g}=-\frac{1}{\rho_g}\frac{\partial P}{\partial x}+\nu_g\frac{\partial^2 u_g}{\partial y_g^2} \tag{4}$$

$$u_g\frac{\partial T_g}{\partial x}+v_g\frac{\partial T_g}{\partial y_g}=\alpha_g\frac{\partial^2 T_g}{\partial y_g^2} \tag{5}$$

$$u_g\frac{\partial \omega}{\partial x}+v_g\frac{\partial \omega}{\partial y_g}=D\frac{\partial^2 \omega}{\partial y_g^2} \tag{6}$$

where the subscript "g" indicates air stream variables and ω, ρ, ν, α and D are the relative humidity, density, kinematic viscosity, thermal diffusivity and mass diffusivity of the air, respectively.

(c) *Corresponding boundary and interface matching conditions*:

At inlet ($x=0$)

$$T_l=T_{l,in},\quad T_g=T_{g,in},\quad u_g=-\frac{1}{2\mu_g}\frac{dP}{dx}(y_g^2-Hy_g),$$
$$\omega=\omega_\infty \tag{7}$$

At wall ($y_l=0$, $y_g=H$)

$$\text{at } y_l=0,\quad u_l=0,\quad T_l=T_w \tag{8}$$
$$\text{at } y_g=H,\quad u_g=0,\quad v_g=0,\quad \partial T_g/\partial y_g=0,\quad \partial\omega/\partial y_g=0$$

At liquid–air interface ($y_l=d$ and $y_g=0$)

$$u_i=u_{l,i}=u_{g,i},\quad T_i=T_{l,i}=T_{g,i} \tag{9}$$

$$v_{g,i}=-\frac{D_g}{1-\omega_i}\left(\frac{\partial\omega}{\partial y_g}\right)_i \tag{10}$$

$$\int_0^H(\rho_g u_{g,in})dy_g+\int_0^x(\rho_g v_{g,i})dx=\int_0^H(\rho_g u_{g,x})dy_g \tag{11}$$

$$\left(\mu_l\frac{\partial u_l}{\partial y_l}\right)_i=\left(\mu_g\frac{\partial u_g}{\partial y_g}\right)_i=\tau_i \tag{12}$$

$$q_t''=-k_e\left(\frac{\partial T_l}{\partial y_l}\right)_i\quad\text{and}\quad q_t''=q_s''+q_l''=-k_g\left(\frac{\partial T_g}{\partial y_g}\right)_i+m_v''h_{fg} \tag{13}$$

For the present case of steady channel flow, Eq. (11) is for the overall mass balance in air steam region. Therefore, at each axial location gives the pressure gradient in the air steam. Meanwhile, Eqs. (12) and (13) yield the continuity of the shear stress and the energy balance at the liquid–air interface, respectively. The total heat flux input at the heated wall, q_t'', is transferred in one of two modes, namely sensible heat flux via the air temperature gradient, q_s'', and latent heat flux via the liquid film vaporization, q_l''.

In the current calculations, the interfacial evaporating mass flux is given by

$$m_v''=\rho_g v_{g,i}=-\frac{\rho_g D_g}{1-\omega_i}\left(\frac{\partial\omega}{\partial y_g}\right)_i \tag{14}$$

The relative humidity (ω_i) is expressed as

$$\omega_i=\frac{M_v P_{v,i}}{M_g p_g} \tag{15}$$

where $P_{v,i}$ is the partial pressure of the saturated vapor at the liquid–air interface. The inlet mass flow rate of the liquid film is given by Bird et al. (1960)

$$m_{l,in}=\frac{\rho_l g}{3\nu_l}d^3\varepsilon^3\cos\varphi \tag{16}$$

The conservation equations can be cast into dimensionless form by adopting the following dimensionless variables

$$X=\frac{x}{H},\quad Y_g=\frac{y_g}{H}\sqrt{Re_g},\quad Y_l=\frac{y_l}{d},\quad \delta=\frac{d}{H},$$
$$U_g=\frac{u_g}{u_{g,ave}},\quad V_g=\frac{v_g}{u_{g,ave}}\sqrt{Re_g},\quad U_l=\frac{u_l}{u_{g,ave}},$$
$$P^*=\frac{P-P_0}{\rho_a u_{g,ave}^2},\quad \theta_g=\frac{T_g-T_{g,\infty}}{T_w-T_{g,\infty}},\quad \theta_l=\frac{T_l-T_{g,\infty}}{T_w-T_{g,\infty}},$$
$$\lambda=\frac{\omega-\omega_\infty}{\omega_w-\omega_\infty} \tag{17}$$

where δ is the ratio of the porous layer thickness to the channel width and ω_w is the relative humidity corresponding to the wall temperature, T_w. Note that the remaining symbols are defined in the nomenclature.

The dimensionless governing equations (corresponding to Eqs. (1)–(6)) are given by

Liquid film region:

$$0=\frac{Re_g\cdot\delta^2}{\nu^*\cdot Fr^2}+\frac{1}{\varepsilon}\frac{\partial^2 U_l}{\partial Y_l^2}-\frac{1}{Da}\cdot U_l-\frac{\Gamma}{Da}\cdot U_l^2 \tag{18}$$

$$U_l\frac{\partial\theta_l}{\partial X}=\frac{\nu^*}{\delta^2 Pr_e Re_g}\frac{\partial^2\theta_l}{\partial Y_l^2} \tag{19}$$

Air stream region:

$$\frac{\partial U_g}{\partial X}+\frac{\partial V_g}{\partial Y_g}=0 \tag{20}$$

$$U_g\frac{\partial U_g}{\partial X}+V_g\frac{\partial U_g}{\partial Y_g}=-\frac{\partial P^*}{\partial X}+\frac{\partial^2 U_g}{\partial Y_g^2} \tag{21}$$

$$U_g\frac{\partial\theta_g}{\partial X}+V_g\frac{\partial\theta_g}{\partial Y_g}=\frac{1}{Pr_g}\frac{\partial^2\theta_g}{\partial Y_g^2} \tag{22}$$

$$U_g\frac{\partial\lambda}{\partial X}+V_g\frac{\partial\lambda}{\partial Y_g}=\frac{1}{Pr_g Le}\frac{\partial^2\lambda}{\partial Y_g^2} \tag{23}$$

where $\nu^*=\nu_l/\nu_g$ is the kinematic viscosity ratio of liquid to air, $Da=K/d^2$ is the Darcy number of the porous medium, and $\Gamma=Cu_{g,ave}\sqrt{K}/\nu_l$ is the dimensionless inertia coefficient of non-Darcian flow. The dimensionless expressions

of Re_g(Reynolds number of air stream), Pr (Prandtl number), Le (Lewis number) and Fr (Froude number) are defined as

$$Re_g = \frac{\rho_g u_{g,ave} H}{\mu_g}, \quad Le = \frac{\alpha_g}{D_g}, \quad Fr = \frac{u_{g,\infty}}{(g\cos\varphi \cdot H)^{1/2}}$$
$$Pr_g = \frac{\nu_g}{\alpha_g}, \quad Pr_e = \frac{\nu_l}{\alpha_e} \tag{24}$$

The corresponding dimensionless boundary conditions are given by

At inlet ($X = 0$):

$$\theta_l = \theta_{l,in}, \quad \theta_g = 0, \quad U_g = \frac{u_{g,in}}{u_{g,ave}}, \quad \lambda = 0 \tag{25}$$

At solid walls:

$$\begin{aligned} &\text{at } Y_l = 0, \quad U_l = 0, \quad \theta_l = 1 \\ &\text{at } Y_g = \sqrt{Re_g}, \quad U_g = 0, \quad V_g = 0, \\ &\partial\theta_g/\partial Y_g = 0, \quad \partial\lambda/\partial Y_g = 0 \end{aligned} \tag{26}$$

At liquid–air interface ($Y_l = 1$):

$$U_l = U_{l,i} = U_{g,i}, \quad \theta_l = \theta_{l,i} = \theta_{g,i} \tag{27}$$

$$V_{g,i} = -\frac{(\omega_{w,in} - \omega_\infty)}{(1-\omega_i)} \frac{1}{Pr_g Le} \left(\frac{\partial\lambda}{\partial Y_g}\right)_i \tag{28}$$

$$\frac{\int_0^H (\rho_g u_{g,ave})\mathrm{d}y_g}{\int_0^H (\rho_g u_{g,x})\mathrm{d}y_g} + \frac{\int_0^x (\rho_g v_{g,i})\mathrm{d}x}{\int_0^H (\rho_g u_{g,x})\mathrm{d}y_g} = 1 \tag{29}$$

$$\left(\frac{\partial U_l}{\partial Y_l}\right)_i = \sqrt{Re_g}\left(\frac{\rho_g}{\rho_l}\right)\frac{1}{\nu^*}\delta\left(\frac{\partial U_g}{\partial Y_g}\right)_i \tag{30}$$

$$\left(\frac{\partial\theta_l}{\partial Y_l}\right)_i = \sqrt{Re_g}\frac{k_g}{k_e}\delta\left(\frac{\partial\theta_g}{\partial Y_g}\right)_i + \sqrt{Re_g}\frac{\rho_g D_g h_{fg}(\omega_{w,in} - \omega_\infty)}{k_e(1-\omega_i)(T_w - T_\infty)}\delta\left(\frac{\partial\lambda}{\partial Y_g}\right)_i \tag{31}$$

The local heat transfer coefficient, $h_{t,x}$, at the liquid–air interface is defined as

$$h_{t,x} = \frac{q''_t}{(T_w - T_{g,\infty})} = \frac{\left(-k_g\frac{\partial T_g}{\partial y_g}\right)_i}{(T_w - T_{g,\infty})} + \frac{m''_v \cdot h_{fg}}{(T_w - T_{g,\infty})} \tag{32}$$

It should be noted that the reference temperature difference in Eq. (32) is specifically defined as $(T_w - T_{g,\infty})$ rather than $(T_i - T_{g,\infty})$ because $(T_i - T_{g,\infty})$ is an unknown and changeable value and is therefore inapplicable for the present non-dimensional analysis. The local Nusselt number along the liquid–air interface is defined as

$$Nu_x = \frac{h_{t,x} \cdot H}{k_g} \tag{33}$$

The average Nusselt number over the length L of the plate is given by

$$Nu = \frac{\int_0^L Nu_x \mathrm{d}x}{L} \tag{34}$$

Incorporating with Eq. (14), the local mass transfer coefficient, $h_{m,x}$, is defined as

$$h_{m,x} = \frac{m''_{v,i}(1-\omega_i)}{\rho_g(\omega_w - \omega_\infty)} \tag{35}$$

The local Sherwood number along the liquid–air interface is defined as

$$Sh_x = \frac{h_{m,x} \cdot H}{D_g} \tag{36}$$

The average Sherwood number over the length L of the plate is written as

$$Sh = \frac{\int_0^L Sh_x \mathrm{d}x}{L} \tag{37}$$

3. Numerical method

The coupled governing equations (Eqs. (18)–(23)) are parabolic in X-direction, and therefore the finite difference solutions for these equations can be marched along the downstream direction from inlet ($X = 0$). In this study, the governing equations are discretized to a fully implicit difference representation, in which the upwind scheme is used to model the axial convective terms, while second-order central difference schemes are employed for the transverse convection and diffusion terms. The Newton linearization procedure is used to linearize the nonlinear terms of Eqs. (18)–(23). In the following, the discretization equations are written in a "block-tridiagonal" form and solved using the tridiagonal matrix method. The current solution procedure is similar to that reported in Han et al. (1978). The flow chart of the numerical procedure is shown schematically in Fig. 2. A grid system of $(I, J, K) = (101, 51, 41)$ grid points is adopted in the computation domain (where I is the total number of grid points along the plate, J is the total number of grid points across the air boundary, and K is the total number of grid points across the liquid film) and the divergence-free criterion is specified as 10^{-5}. A careful check for the grid-independence of the numerical solutions is performed to ensure the accuracy and validity of the numerical results. The grid-independence check is performed using five grid systems $201 \times (81 + 66)$, $101 \times (81 + 66)$, $101 \times (51 + 41)$, $101 \times (36 + 26)$ and $51 \times (36 + 26)$ for the specific case of $Re_g = 500$, $\varepsilon = 0.4$, $\delta = 0.2$, $\varphi = 0$ and $\phi = 70\%$. Table 1 presents the average Nusselt and Sherwood numbers obtained for each of these five grid systems and calculates their error relative to the results obtained using the $201 \times (81 + 66)$ grid system.

4. Results and discussion

This study investigates the effect of introducing a liquid-saturated porous material on the heat and mass transfer performance of an evaporating liquid film flow within an airflow channel. Specifically, the coupled effects of the porosity (ε) and the porous layer thickness (δ) on the local

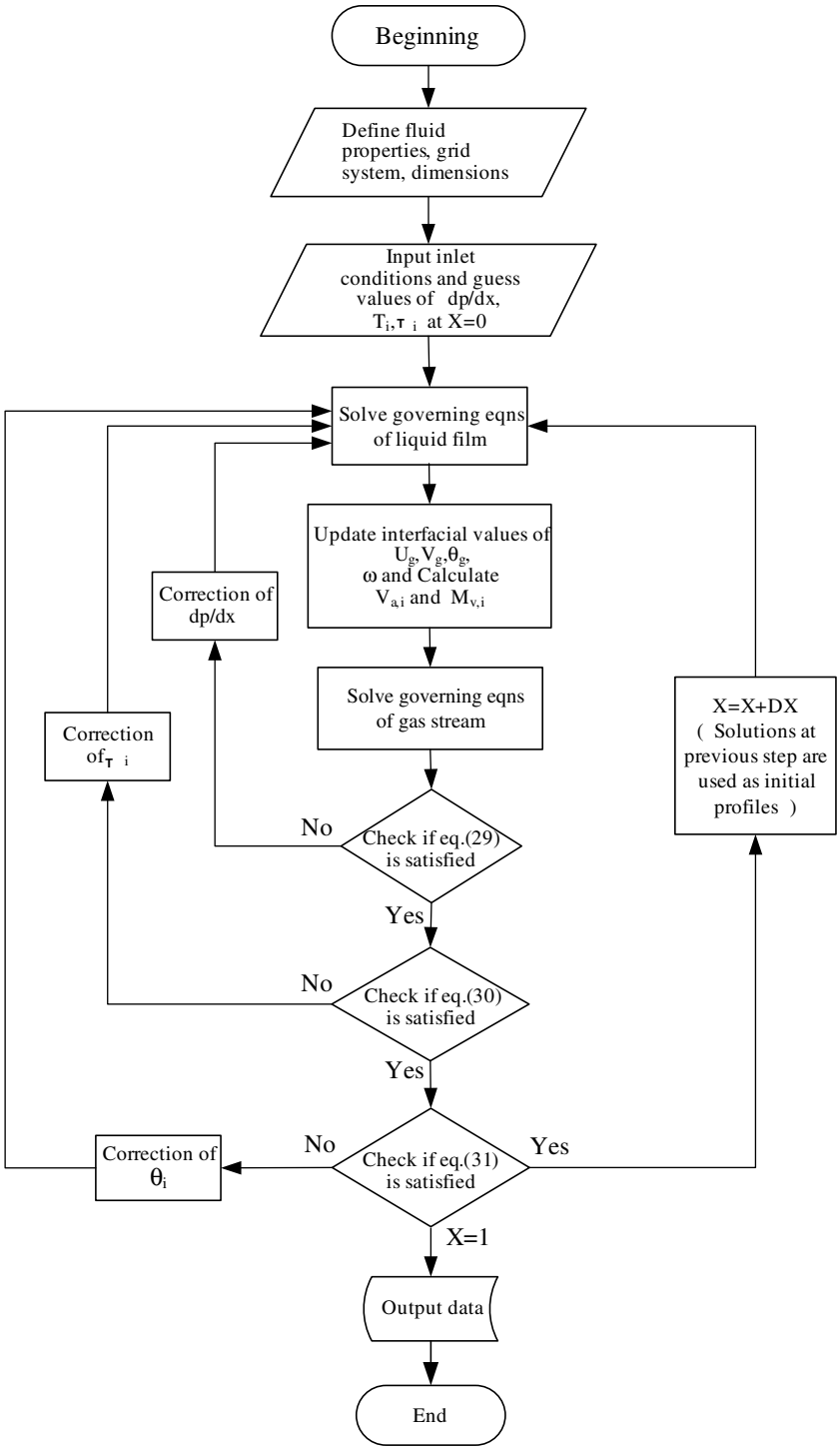

Fig. 2. Flow chart of numerical procedure.

transport phenomena and average heat and mass transfer performances are investigated for air flows with Reynolds numbers (Re_g) ranging from 300 to 900 ($u_{g,ave} = 0.1 \sim 0.3\ m\ s^{-1}$). In accordance with a typical practical application, the numerical simulations assume the following conditions: $P_\infty = 1$ atm, $T_w = 60$ °C, $T_{l,in} = T_{g,\infty} = 27$ °C, $L = 0.5$ m, and $H = 0.05$ m. Furthermore, it is assumed that the liquid and air are water and humid air, respectively.

Fig. 3 presents the axial distribution of the dimensionless liquid–air interfacial temperature (θ_i) for selected values of Re_g ($Re_g = 500$, 900) and ε ($\varepsilon = 0.4$, 0.8, 1.0) at $\delta = 0.2$, $\varphi = 0$ and $\phi = 70\%$. Note that the results obtained for $\varepsilon = 1$ correspond to the case where the porous medium is not present, and are achieved at $\Gamma = 0$ and $Da \to \infty$. It can be seen that θ_i initially increases rapidly with the axial location X, but then remains virtually constant after $X = 2$. Additionally, it is found that the value of θ_i reduces as Re_g

Table 1
Comparison of average *Nu* and *Sh* numbers for five grid systems at $Re_g = 500$, $\varepsilon = 0.4$, $\delta = 0.2$, $\varphi = 0$ and $\phi = 70\%$

Grid systems	*Nu*		*Sh*	
	Value	Relative error (%)	Value	Relative error (%)
$201 \times (81 + 66)$	55.56	–	3.29	–
$101 \times (81 + 66)$	55.11	0.81	3.26	0.91
$101 \times (51 + 41)$	56.14	1.04	3.33	1.22
$101 \times (36 + 26)$	58.41	5.13	3.48	5.78
$51 \times (36 + 26)$	57.71	3.80	3.43	4.26

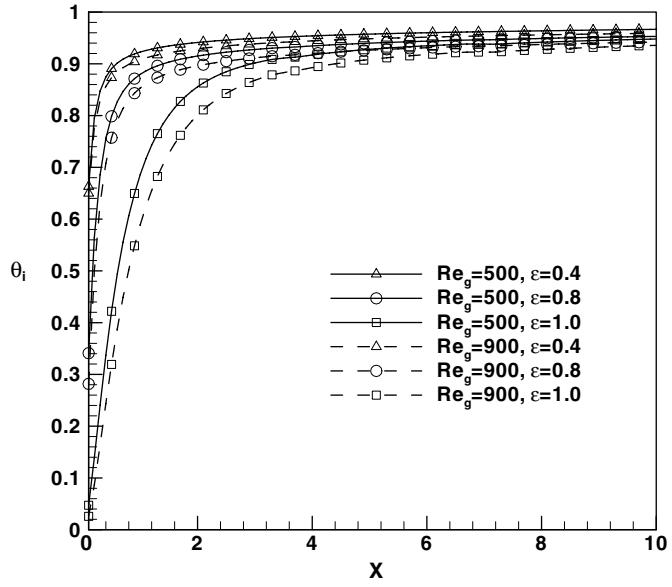

Fig. 3. Axial distribution of dimensionless interfacial temperature for various Re_g and ε with $\delta = 0.2$, $\varphi = 0$ and $\phi = 70\%$.

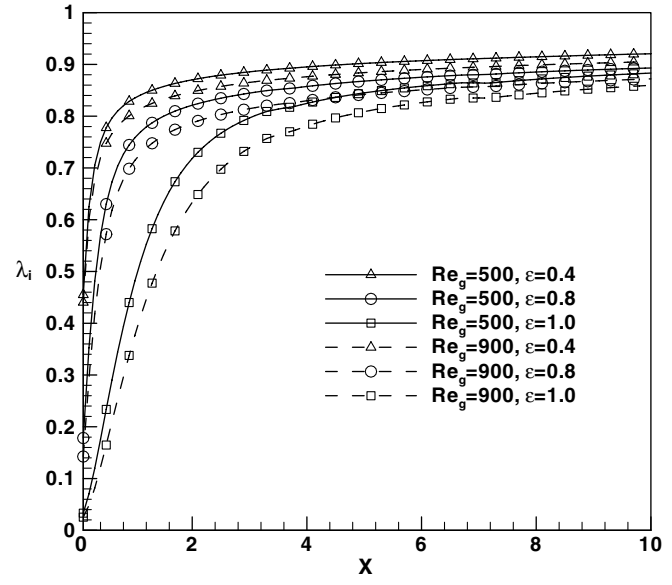

Fig. 4. Axial distribution of dimensionless interfacial mass concentration for various Re_g and ε with $\delta = 0.2$, $\varphi = 0$ and $\phi = 70\%$.

increases, which confirms the general concept that both the heat and the mass transfer rates are enhanced in airstreams with higher Reynolds numbers. The results also show that the interfacial temperature increases as the porosity decreases. This implies that the introduction of the liquid-saturated porous layer increases the liquid–air interfacial temperature. The reason for this is that the porous layer increases the heat transfer area of the liquid film and hence promotes heat transfer into the liquid film.

Figs. 4 and 5 present the axial distributions of the dimensionless mass concentration (λ_i) and liquid evaporation rate (m''_v), respectively. The axial distribution of λ_i follows the same trend as that of θ_i shown in Fig. 3 since a higher interfacial temperature results in a higher mass concentration. It is observed that λ_i increases with reducing ε

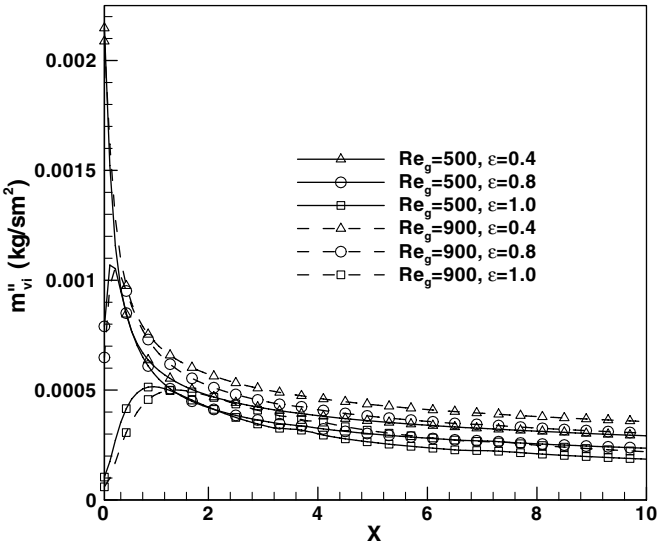

Fig. 5. Evaporating flux of liquid at each axial location for various Re_g and ε with $\delta = 0.2$, $\varphi = 0$ and $\phi = 70\%$.

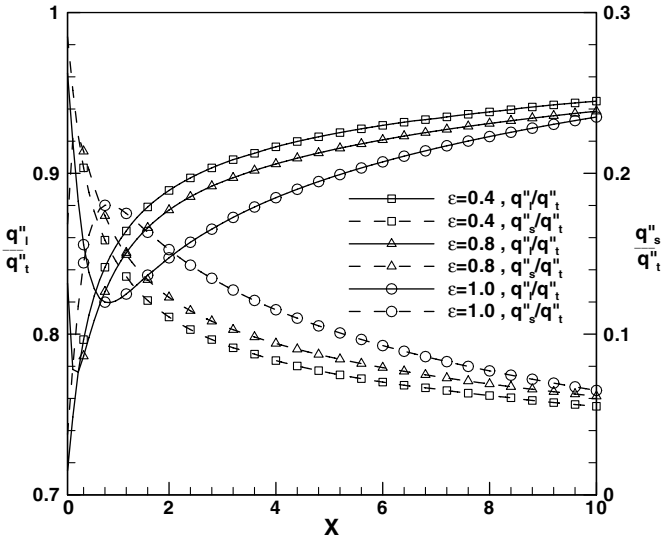

Fig. 6. Axial distribution of latent heat flux (q_l/q_t) and sensible heat flux (q_s/q_t) for various ε with $Re_g = 500$, $\delta = 0.2$, $\varphi = 0$ and $\phi = 70\%$.

and Re_g. However, comparing Figs. 3 and 4, it is noted that ε and Re_g exert a greater effect on the mass concentration than on the interfacial temperature. Fig. 5 shows the axial distribution of the liquid evaporation rate (m''_v) at various values of ε and Re_g. It is apparent that the liquid film vaporization rate increases as ε reduces or as Re_g increases since a higher interfacial temperature gradient generates a higher concentration gradient at the interface.

In liquid film evaporation, heat transfer is achieved by both sensible and latent heat transfer mechanisms. This study evaluates the influence of porous structures on both heat transfer mechanisms. Fig. 6 presents the axial distributions of the latent and sensible heat transfer rates (q''_l/q''_t and q''_s/q''_t, respectively) for various values of $\varepsilon(\varepsilon = 0.4, 0.8, 1.0)$ at $Re_g = 500$, $\delta = 0.2$, $\varphi = 0$ and $\phi = 70\%$. From inspection, it is found that latent heat transfer accounts for approximately 74–95% of the total heat transfer. It is also noted that a lower value of ε results in a higher latent heat transfer rate (q''_l/q''_t) and a lower sensible heat transfer rate (q''_s/q''_t). In other words, a porous layer with a lower porosity increases the relative contribution of latent heat transfer.

Fig. 7(a) and (b) present the variations of the average Nusselt (Nu) number and Sherwood (Sh) number, respectively, with Re_g for different values of $\varepsilon(\varepsilon = 0.4, 0.8, 1.0)$ at $\delta = 0.2$, $\varphi = 0$ and $\phi = 70\%$. As expected, Nu and Sh

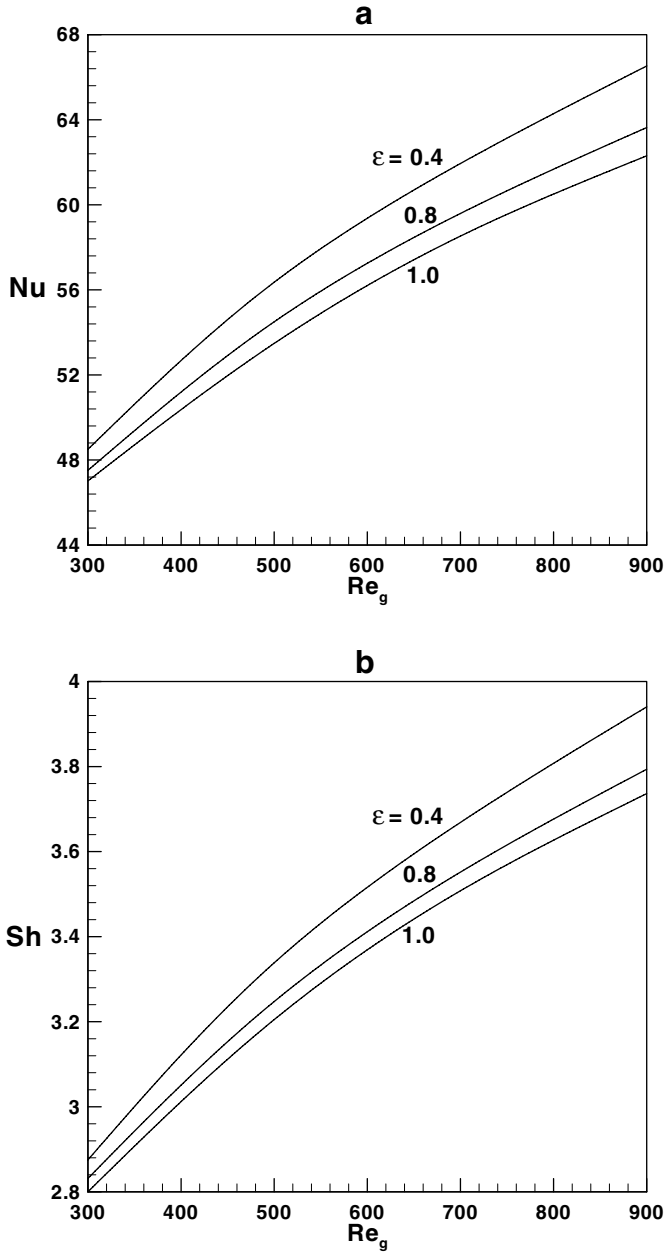

Fig. 7. Variation of average (a) Nusselt number and (b) Sherwood number with Re_g for various ε at $\delta = 0.2$, $\varphi = 0$ and $\phi = 70\%$.

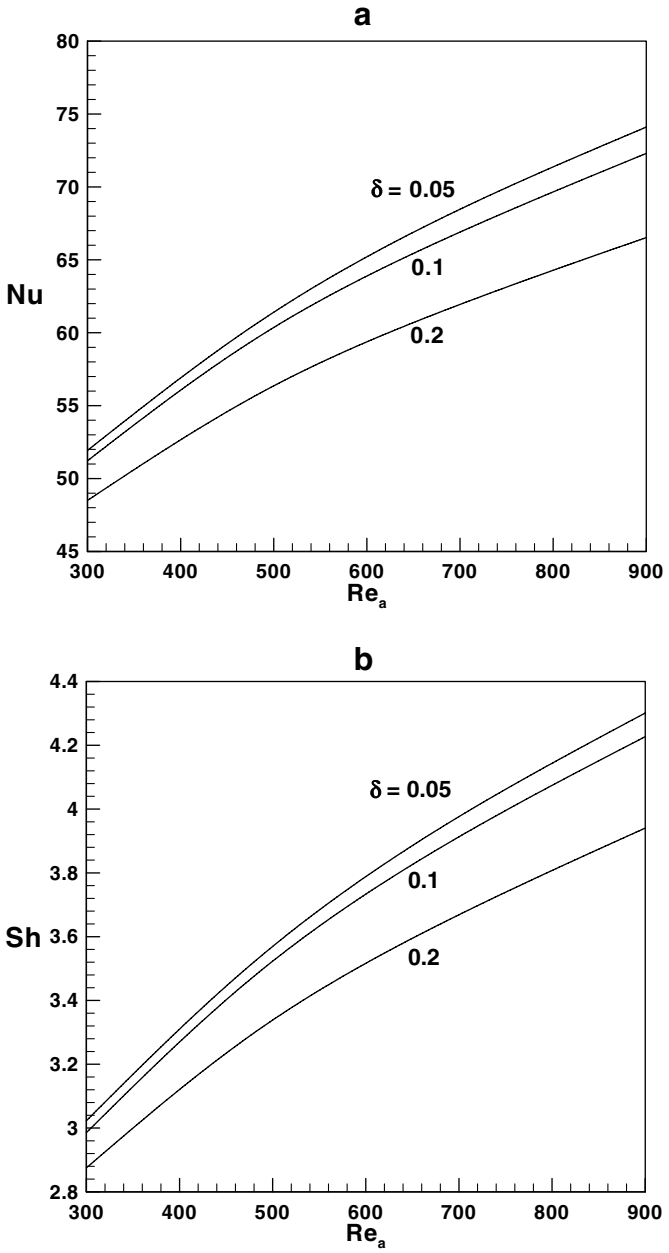

Fig. 8. Variation of average (a) Nusselt number and (b) Sherwood number with Re_g for various δ at $\varepsilon = 0.4$, $\varphi = 0$ and $\phi = 70\%$.

both increase with increasing Re_g. Additionally, a lower porosity increases both *Nu* and *Sh*. It is observed that the influence of the porosity on *Nu* and *Sh* becomes more significant as Re_g increases. Specifically, for a constant $Re_g = 900$, *Nu* and *Sh* are increased by 8% and 7%, respectively, for $\varepsilon = 0.4$ compared to their values at $\varepsilon = 1.0$ (i.e. no porous medium).

Fig. 8(a) and (b) illustrate the effect of the porous layer thickness ($\delta = 0.05$, 0.1 and 0.2) on the heat and mass transfer performance of liquid film evaporation for various values of Re_g with $\varepsilon = 0.4$, $\varphi = 0$ and $\phi = 70\%$. It is observed that larger values of *Nu* and *Sh* are obtained for a lower δ since a thicker porous layer causes a significant reduction in the interfacial temperature and hence reduces the quantity of evaporative vapor.

Fig. 9(a) and (b) show the coupled effects of ε and the inclined angle φ(0°, 60°and 90°, where $\varphi = 0°$ indicates a vertical parallel plate) on *Nu* and *Sh*, respectively, for $Re_g = 500$, $\delta = 0.2$ and $\phi = 70\%$. It can be seen that *Nu* and *Sh* increase with decreasing ε. Furthermore, larger values of *Nu* and *Sh* are obtained at lower inclined angles since the average velocity of the liquid increases as the inclined angle decreasing and this reduces heat transfer in the *Y*-direction, which in turn causes a lower temperature and mass concentration at the air–liquid interface. It is observed that the influence of the porosity (ε) on the heat

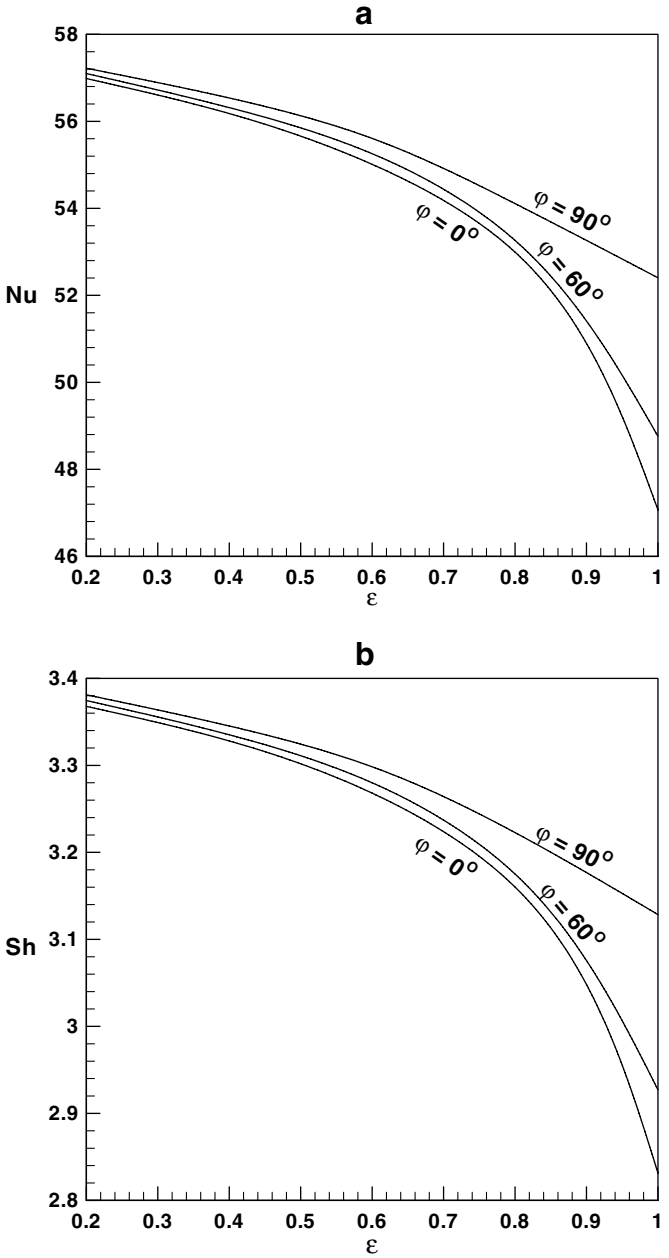

Fig. 9. Coupled effects of porosity ε and inclined angle φ on average (a) Nusselt number and (b) Sherwood number with $Re_g = 500$ and $\phi = 70\%$.

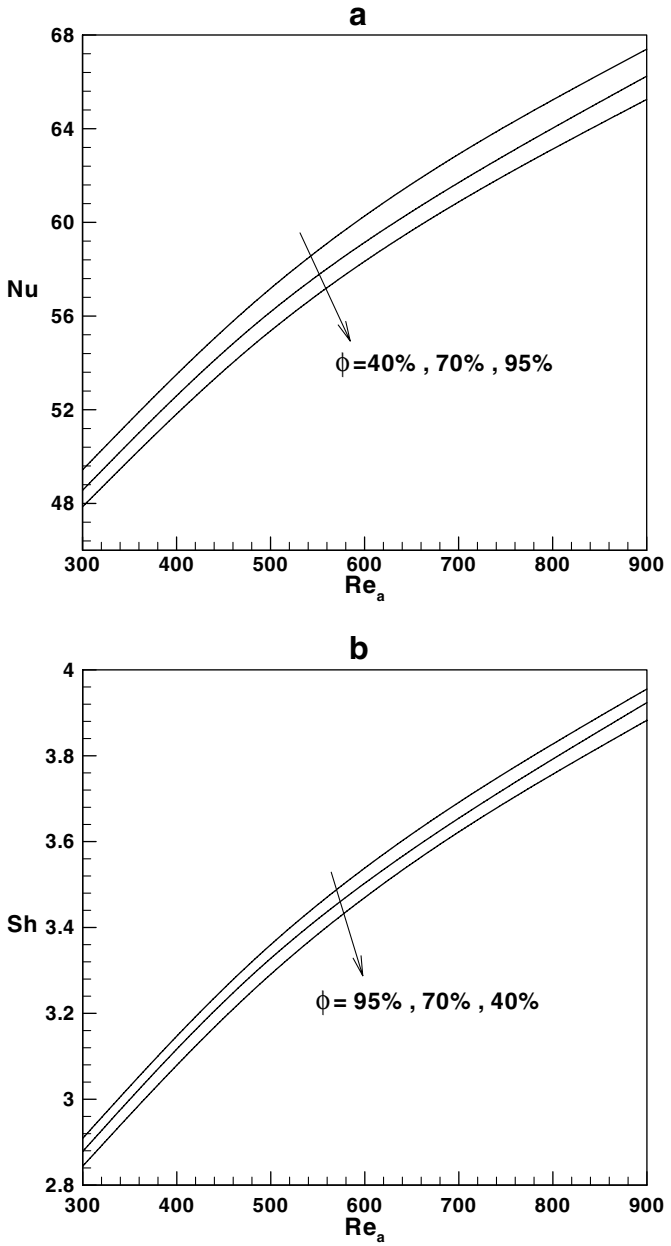

Fig. 10. Variation of average (a) Nusselt number and (b) Sherwood number with Re_g for various ϕ at $\varepsilon = 0.4$, $\varphi = 0$ and $\delta = 0.2$.

and mass transfer performance is not significant when the porosity ε is small ($\varepsilon < 0.4$). However, the effect of the inclined angle on the heat and mass transfer becomes more pronounced at higher porosities.

Fig. 10(a) and (b) illustrate the influence of the ambient relative humidity (ϕ) on *Nu* and *Sh*, respectively. From Fig. 10(a), it is apparent that the Nusselt number increases with decreasing ϕ. This is because a higher mass concentration difference exists between the liquid–air interface and the air stream at a lower ambient relative humidity, and this prompts a higher mass flow rate. However, an opposite trend is apparent for the Sherwood number, i.e. *Sh* reduces with decreasing ϕ. This anomaly arises from the greater effect of ϕ on the mass concentration difference ($\omega_w - \omega_\infty$) in Eq. (35) than on the evaporation rate m''_v. To investigate the double diffusion behavior at the liquid–air interface in more detail, the variations of the Nusselt and Sherwood numbers with Re_g are plotted in Fig. 11(a) and (b), respectively, for selected Lewis numbers ($Le = 0.1$, 1.0, 10) at $\varepsilon = 0.4$, $\delta = 0.01$ and $\phi = 70\%$. The Lewis number ($Le = \alpha/D$) indicates the relative extent of the temperature and concentration fields from the interface. As the Lewis number increases ($Le > 1$), the concentration boundary layer becomes thinner relative to the thermal boundary layer. It is reasonable to expect that this leads to a higher mass flow rate and heat transfer rate. This inference is consistent with the results of Fig. 11(a) and (b), which show that *Nu* and *Sh* both increase with increasing *Le*.

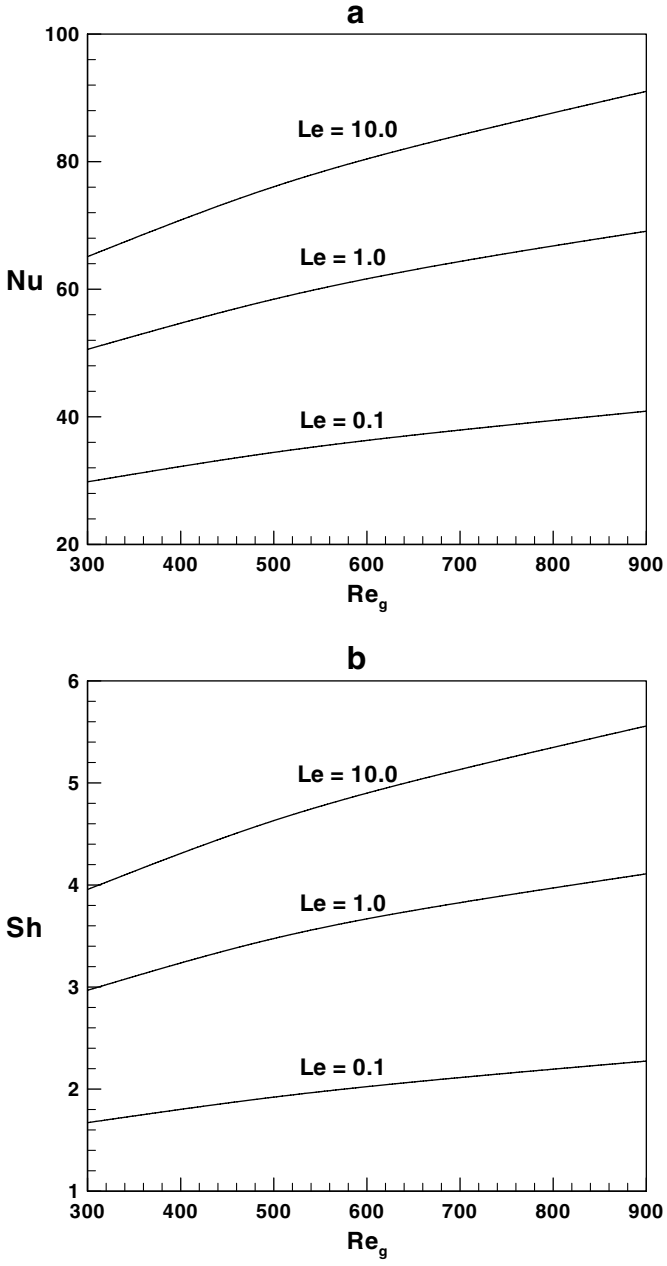

Fig. 11. Variation of average (a) Nusselt number and (b) Sherwood number with Re_g for various Lewis numbers with $\varepsilon = 0.4$, $\delta = 0.2$, $\varphi = 0$ and $\phi = 70\%$.

5. Conclusion

The present study has explored the heat and mass transfer enhancement of liquid film evaporation obtained by introducing a liquid-saturated porous layer within an inclined flow channel. The axial distributions of θ_i, λ_i, m''_v, q''_l/q''_t and q''_s/q''_t versus Re_g for selected values of ε, δ and ϕ have been numerically described. In addition, the effects of ε, δ, φ, ϕ and *Le* on the average heat and mass transfer performance have been examined. The numerical results have shown that latent heat flux is the dominant heat transfer mode in the present study. Lower values of ε and δ yield higher interfacial temperatures and mass concentrations, and therefore enhance the heat and mass transfer performance across the liquid-film interface. The influence of ε on *Nu* and *Sh* becomes gradually more significant as φ is decreased. Regarding the effect of the ambient relative humidity (ϕ), it has been observed that a lower value of ϕ increases *Nu* but reduces *Sh*. However, the influence of ϕ on *Nu* and *Sh* is less significant than that of ε and δ. Finally, it has been shown that the heat and mass transfer rates are improved as the Lewis number increases ($Le > 1$).

References

Alazmi, B., Vafai, K., 2000. Analysis of variants within the porous media transport models. ASME J. Heat Transfer-Trans. 122 (2), 303–326.

Baumann, W.W., Thiele, F., 1990. Heat and mass transfer in evaporating two-component liquid film flow. Int. J. Heat Mass Transfer 33, 267–273.

Bird, R.B., Stewant, W.E., Lightfoot, E.N., 1960. Transport Phenomena. John Wiely & Sons, New York (Chapter 2).

Chen, T.S., Yuh, C.F., 1979. Combined heat and mass transfer in natural convection on inclined surfaces. Numer. Heat Transfer 2, 233–250.

Diky, N.A., Koloskova, N.Y., Tuz, V.E., Dubrovskaya, V.V., 1996. Heat and mass transfer and hydrodynamics of liquid evaporation in contact apparatus with a porous packing. Exp. Therm. Fluid Sci. 13, 85–91.

Dowson, D.A., Trass, O., 1972. Mass transfer at rough surfaces. Int. J. Heat Mass Transfer 15, 1317–1336.

Gebhart, B., Pera, L., 1971. The nature of vertical natural convection flows resulting from the combined buoyancy effects of thermal and mass diffusion. Int. J. Heat Mass Transfer 14, 2028–2050.

Han, J.C., Glicksman, L.R., Rohsenow, W.M., 1978. An investigation of heat transfer and friction for rib-roughened surfaces. Int. J. Heat Mass Transfer 21, 1143–1156.

Kozlu, H., Mikic, B.B., Patera, A.T., 1992. Turbulent heat transfer augmentation using microscale disturbances inside the viscous sublayer. ASME J. Heat Transfer 114, 348–353.

Maclaine-Cross, I.L., Banks, P.J., 1972. Coupled heat and mass transfer in regenerators-prediction using an analogy with heat transfer. J. Heat Mass Transfer 15, 1225–1242.

Maclaine-Cross, I.L., Banks, P.J., 1981. A general theory of wet surface heat exchangers and its application to regenerative evaporative cooling. ASME J. Heat Transfer 103, 579–585.

Mezaache, E., Daguenet, M., 2005. Effects of inlet conditions on film evaporation along an inclined plate. Solar Energy 78, 535–542.

Peres-Blanco, H., Bird, W.A., 1984. Study of heat and mass transfer in a vertical-tube evaporative cooler. ASME J. Heat Transfer 106, 210–215.

Shembharkar, T.R., Pai, B.R., 1986. Prediction of film cooling with a liquid coolant. Int. J. Heat Mass Transfer 29, 899–908.

Tsay, Y.L., 1995. Heat transfer enhancement through liquid film evaporation into countercurrent moist air flow in a vertical plate channel. Heat Mass Transfer 30, 473–480.

Wassel, A.T., Mills, A.F., 1987. Design methodology for a countercurrent falling film evaporative condenser. ASME J. Heat Transfer 109, 784–787.

Yan, W.M., Lin, T.F., 1991. Evaporative cooling of liquid film through interfacial heat and mass transfer in a vertical channel—II Numerical study. Int. J. Heat Mass Transfer 34, 1113–1124.

Yan, W.M., Soong, C.Y., 1995. Convection heat and mass transfer along an inclined heated plate with film evaporation. Int. J. Heat Mass Transfer 38, 1261–1269.

Zhao, T.S., 1999. Coupled heat and mass transfer of a stagnation point flow in a heated porous bed with liquid film evaporation. Int. J. Heat Mass Transfer 42, 861–872.

Zheng, G.S., Worek, W.M., 1996. Method of heat and mass transfer enhancement in film evaporation. Int. J. Heat Mass Transfer 39, 97–108.